ELSEVIER

Engineering Analysis with Boundary Elements 25 (2001) 297–311

ENGINEERING ANALYSIS *with* BOUNDARY ELEMENTS

www.elsevier.com/locate/enganabound

Regularized spectral multipole BEM for plane elasticity

J.D. Richardson[a,*], L.J. Gray[a], T. Kaplan[a], J.A.L. Napier[b]

[a]*Computer Science and Mathematics Division, Oak Ridge National Laboratory, Oak Ridge, TN 37831-6367, USA*
[b]*CSIR Division of Mining Technology, P.O. Box 91230, Auckland Park 2006 Johannesburg, South Africa*

Abstract

A multipole algorithm for plane elasticity based on the direct boundary element method (BEM) is presented. The kernels in the BEM are approximated as truncated Taylor series with expansion points taken from a uniform grid. The algorithm replaces the usual BEM elemental summations with correlation sums on the regular grid in terms of the sampled kernel data and density moments. Far field influences are rapidly computed in the frequency domain using the fast Fourier transform (FFT). The resultant linear system of equations is solved with GMRES. The multipole method is extended to whole-body regularized forms of the standard displacement-BIE and the stress-BIE. Free-term coefficients which arise from regularization in the far field are also rapidly computed as correlation sums with the FFT. The algorithm is shown to be faster than the traditional BEM for models with over 400 quartic elements while maintaining an acceptably high level of accuracy. © 2001 Elsevier Science Ltd. All rights reserved.

Keywords: Boundary element method; Elasticity; Multipole; Regularization; Hypersingular; Fast Fourier transform

1. Introduction

It is generally recognized that the boundary element method (BEM) can offer significant computational savings compared to numerical methods which involve domain discretizations. In addition to the obvious reduction in dimensionality of the discretized geometry, increased efficiency in the BEM is also largely due to the fact that, for a given level of accuracy, BEM models can successfully employ discretizations, which are much coarser than discretizations required in domain methods. However, for the class of problems in which the discretization level is predominantly determined by the presence of many fine surface details, there is a large expense for computing and solving the dense matrices associated with BEM systems. Nonetheless, the BEM is still likely to be the preferred modeling choice over several alternative approaches since the method can offer key advantages even for large systems. In particular, the superior accuracy of the BEM for linear elastic fracture modeling and its obvious advantages for problems which require numerous mesh updates make it desirable to find ways to extend the effective range of the BEM.

Methods used to extend the BEM to large scale systems may be considered as either modeling strategies or algorithmic strategies. The primary modeling strategy is the multi-zone method [1]. In the multi-zone method, virtual interior surfaces are introduced so that the original domain is decomposed into some number of subdomains. The BEM is then applied to each subdomain using coupled boundary conditions between adjacent subdomains. Early applications of the method served as a means to extend the system size which could be handled effectively [2,3]. More recent algorithms have used parallel implementation [4], an adaptation for which the approach is particularly well-suited. The multi-zone method results in a blocked-sparse system of increased rank compared to the traditional BEM. When the increase in system size is not too great and the maximum block size is small enough, multi-zone methods offer large computational savings over traditional BEM approaches. A possible drawback to the use of multi-zones is the need to reconstruct the virtual surfaces in dynamic simulations, which is similar to the local re-discretization incumbrance associated with domain methods.

The algorithmic strategies used to extend the BEM to large scale problems are based on some type of fast summation method (FSM) [5]. Physical systems described through the use of a potential often require a calculation of the interaction between each component of the system and the remaining components in the system. The method sometimes referred to as the naive approach [6] generates a system of equations by computing $N-1$ influences for each of N components, resulting in an operation count which scales as $O(N^2)$. An FSM is able to compute the $O(N^2)$ system interactions in less than $O(N^2)$ operations. The computational savings is typically gained through

* Corresponding author. Tel.: +1-865-241-3972; fax: +1-865-574-0680.
E-mail address: richardsonj@ornl.gov (J.D. Richardson).

0955-7997/01/$ - see front matter © 2001 Elsevier Science Ltd. All rights reserved.
PII: S0955-7997(01)00028-5

some grouping of influences or decoupling method, which allows some of the source point and field point data to be processed separately.

One of the early FSM algorithms [7] was based on grouped influences for systems of particles and used a recursive domain subdivision technique in which cells at each level used a single particle to represent the center of mass of the enclosed particles. A more recent strategy used to model problems from the electronics industry [8] has been to employ a local collocation scheme to approximate enclosed charges as point charges on a regular grid to facilitate rapid summation with the fast Fourier transform (FFT).

The class of FSM techniques which has come to be known as the fast multipole method (FMM) forms the basis for the present work. The FMM was developed for large-scale discretizations for integral equations in potential theory [9] and later extended to particle simulations [10]. Subsequent researchers have refined and merged aspects of the earlier FSM algorithms. Some two-dimensional applications include algorithms for Stokes flow [11,12], electrostatics in heterogeneous media [13], and fracture simulations for granular assemblies [14]. Three-dimensional multipole algorithms have been developed for potential theory and include the extension of the original FMM [15] and an algorithm for insulated cracks in conducting media [16].

The algorithm described herein belongs to a class of FSM algorithms which comprise the spectral multipole method (SMM) [14,17]. The essence of these algorithms is that elemental summations in the BEM are first written using truncated Taylor series expansions for the kernel functions centered on expansion points from a uniform grid. Elemental sums are expressed as grid summations involving the sampled kernel data and density moments which are either convolution or correlation sums depending on the forms chosen for the kernels. Elemental influences in the far field are then rapidly computed using the FFT and the appropriate theorem for discrete transforms. The computational efficiency stems from the fact that the kernel data and density moments are decoupled, processed separately, and then efficiently summed. The $O(N^2)$ effort to compute the system matrix is replaced by the computation of only the near field influences, an effort which scales nearly as $O(N)$. The $O(N^2)$ operations for matrix-vector multiplications are reduced to $O(N\log N)$ using the FFT. Finally, for large systems, iterative solvers may be expected to be faster than direct solvers.

The present work is an extension of the SMM to the direct BEM approach. The algorithm is based on whole-body regularized BIEs and computes all free-term coefficients using $O(N\log N)$ operations. A basic description of the algorithm follows after which a pair of examples from two-dimensional linear elasticity will be given to demonstrate the accuracy and efficiency of the method.

2. Regularized boundary integral equations

The Somigliana displacement identity (SDI) and the Somigliana stress identity (SSI) are the bases for integral representations of problems in linear elasticity [18]. The identities give the displacement vector u_l and the stress tensor σ_{kl} at interior points $\mathbf{p}$ as integrals involving the tractions t_i and displacements over the bounding surface denoted by the points $\mathbf{Q}$. The SDI and the SSI can be respectively written in the following forms.

$$u_l(\mathbf{p}) = -\int_S \tilde{\sigma}_{lij}(\mathbf{p},\mathbf{Q})u_i(\mathbf{Q})n_j(\mathbf{Q})\,\mathrm{d}S(\mathbf{Q}) + \int_S U_{li}(\mathbf{p},\mathbf{Q})t_i(\mathbf{Q})\,\mathrm{d}S(\mathbf{Q}), \tag{1}$$

$$\sigma_{kl}(\mathbf{p}) = -\int_S V_{kijl}(\mathbf{p},\mathbf{Q})u_i(\mathbf{Q})n_j(\mathbf{Q})\,\mathrm{d}S(\mathbf{Q}) - \int_S \tilde{\sigma}_{ikl}(\mathbf{p},\mathbf{Q})t_i(\mathbf{Q})\,\mathrm{d}S(\mathbf{Q}). \tag{2}$$

In a slight departure from traditional forms of the SDI and SSI, the surface normal vector $n_j(\mathbf{Q})$ is isolated from two of the kernel functions as part of the formulation required for use with the present multipole scheme. Also based on computational considerations, the ordering of the indices in the same two kernels has been chosen so that the second and third indices in these kernels are summed with the displacement and normal vectors, respectively. The kernel U_{li} is a tensor of displacements corresponding to the Kelvin solution for an orthogonal set of point loads and the strongly singular kernel $\tilde{\sigma}_{lij}$ is the fundamental stress associated with the Kelvin solution and appears in both the SDI and the SSI. The kernel V_{kijl} follows from differentiation of the strongly singular kernel and is therefore hypersingular. The singular and hypersingular integrals must be given special interpretations as an interior point approaches the boundary $\mathbf{p} \to \mathbf{P}$. The interpretation may use direct limit procedures [19,20], finite parts [21,22], or regularization [23,24,25] (see also the recent compilation [26]). The present strategy is to base the BEM on regularized forms of the BIE [24] so that the algorithm can exclusively employ numerical integration.

States of constant stress equal to the boundary stress at $\mathbf{P}$ can be used to regularize the integral equations [25]. The displacements and tractions associated with the constant stress states have the following form,

$$u_k^L(\mathbf{P},\mathbf{Q}) = u_k(\mathbf{P}) + u_{k,m}(\mathbf{P})[x_m(\mathbf{Q}) - x_m(\mathbf{P})] \tag{3}$$

$$t_k^L(\mathbf{P},\mathbf{Q}) = \sigma_{mk}(\mathbf{P})n_m(\mathbf{Q}) \tag{4}$$

and are denoted with the superscript L to indicate their association with a linear displacement field. A rigid body stress-free translation is included in the linear state displacement field. Subtraction of the BIE representations for the

linear states yields the following weakly-singular BIEs.

$$0 = -\int_S \tilde{\sigma}_{lij}(\mathbf{P},\mathbf{Q})[u_i(\mathbf{Q}) - u_i^L(\mathbf{P},\mathbf{Q})]n_j(\mathbf{Q})\,\mathrm{d}S(\mathbf{Q}) + \int_S U_{li}(\mathbf{P},\mathbf{Q})[t_i(\mathbf{Q}) - t_i^L(\mathbf{P},\mathbf{Q})]\,\mathrm{d}S(\mathbf{Q}), \quad (5)$$

$$0 = -\int_S V_{kijl}(\mathbf{P},\mathbf{Q})[u_i(\mathbf{Q}) - u_i^L(\mathbf{P},\mathbf{Q})]n_j(\mathbf{Q})\,\mathrm{d}S(\mathbf{Q}) - \int_S \tilde{\sigma}_{ikl}(\mathbf{P},\mathbf{Q})[t_i(\mathbf{Q}) - t_i^L(\mathbf{P},\mathbf{Q})]\,\mathrm{d}S(\mathbf{Q}). \quad (6)$$

As discussed in [25] the previous results are only meaningful at boundary points where the stress tensor is continuous. It should be recognized that the weakly singular equations given as Eqs. (5) and (6) are based on an $O(r^2)$ displacement field as the regularizing state is extended over the entire surface. The key computational difference between the whole-body regularized BIE's and other BIE forms will be discussed briefly in Section 4.1.

The whole-body regularized BIE's have some attractive features for use in BEM algorithms. Since analytic integration is not required, the extension to three dimensions and the incorporation of any differentiable interpolation into the algorithm are trivial. The BEM implementation requires no special consideration for corners subjected to continuous stress [27]. Finally, the fact that the standard BIE and its gradient appear in nearly similar forms is particularly convenient for programming.

In order to use the weakly singular BIE's within a multipole scheme, the integrals need to be rewritten to isolate the three types of terms to be computed, near field integrals, remote integrals, and free terms involving the boundary data which arise from the regularization. Isolating a local portion of the surface denoted as S_L, the weakly singular displacement-BIE may be rearranged as follows.

$$\begin{aligned}
0 &= -\int_{S-S_L} [u_i(\mathbf{Q}) - u_i^L(\mathbf{P},\mathbf{Q})]\tilde{\sigma}_{lij}(\mathbf{P},\mathbf{Q})n_j(\mathbf{Q})\,\mathrm{d}S(\mathbf{Q}) \\
&\quad - \int_{S_L} [u_i(\mathbf{Q}) - u_i^L(\mathbf{P},\mathbf{Q})]\tilde{\sigma}_{lij}(\mathbf{P},\mathbf{Q})n_j(\mathbf{Q})\,\mathrm{d}S(\mathbf{Q}) \\
&\quad + \int_{S-S_L} [t_i(\mathbf{Q}) - \sigma_{im}(\mathbf{P})n_m(\mathbf{Q})]U_{li}(\mathbf{P},\mathbf{Q})\,\mathrm{d}S(\mathbf{Q}) \\
&\quad + \int_{S_L} [t_i(\mathbf{Q}) - \sigma_{im}(\mathbf{P})n_m(\mathbf{Q})]U_{li}(\mathbf{P},\mathbf{Q})\,\mathrm{d}S(\mathbf{Q}) \\
&= -\int_{S_L} [u_i(\mathbf{Q}) - u_i^L(\mathbf{P},\mathbf{Q})]\tilde{\sigma}_{lij}(\mathbf{P},\mathbf{Q})n_j(\mathbf{Q})\,\mathrm{d}S(\mathbf{Q}) \\
&\quad + \int_{S_L} [t_i(\mathbf{Q}) - \sigma_{im}(\mathbf{P})n_m(\mathbf{Q})]U_{li}(\mathbf{P},\mathbf{Q})\,\mathrm{d}S(\mathbf{Q}) \\
&\quad - \int_{S-S_L} u_i(\mathbf{Q})\tilde{\sigma}_{lij}(\mathbf{P},\mathbf{Q})n_j(\mathbf{Q})\,\mathrm{d}S(\mathbf{Q}) \\
&\quad + \int_{S-S_L} t_i(\mathbf{Q})U_{li}(\mathbf{P},\mathbf{Q})\,\mathrm{d}S(\mathbf{Q}) \\
&\quad + u_i(\mathbf{P})\int_{S-S_L} \tilde{\sigma}_{lij}(\mathbf{P},\mathbf{Q})n_j(\mathbf{Q})\,\mathrm{d}S(\mathbf{Q}) \\
&\quad + u_{i,m}(\mathbf{P})\int_{S-S_L} [x_m(\mathbf{Q}) - x_m(\mathbf{P})]\tilde{\sigma}_{lij}(\mathbf{P},\mathbf{Q})n_j(\mathbf{Q})\,\mathrm{d}S(\mathbf{Q}) \\
&\quad - \sigma_{im}(\mathbf{P})\int_{S-S_L} n_m(\mathbf{Q})U_{li}(\mathbf{P},\mathbf{Q})\mathrm{d}S(\mathbf{Q}) \\
&= u_l^{\mathrm{LC}}(\mathbf{P}) + u_l^{\mathrm{RI}}(\mathbf{P}) + u_i(\mathbf{P})F\mathrm{I}_{li} + u_{i,m}(\mathbf{P})F\mathrm{II}_{mli} \\
&\quad - \sigma_{im}(\mathbf{P})F\mathrm{III}_{mli}. \quad (7)
\end{aligned}$$

The term representing the sum of the integrals on S_L is denoted with a superscript 'LC' in the last line of the equation to denote a local contribution. The usual integrals over the non-local surface $S - S_L$, are denoted with a superscript 'RI' in the final line of the equation to indicate that they represent a remote influence. It is these remote influence integrals which are to be computed indirectly through the use of multipoles. The integrals which multiply the free-term displacement, displacement gradient, and stress are respectively denoted as $F\mathrm{I}_{li}$, $F\mathrm{II}_{mli}$, and $F\mathrm{III}_{mli}$ in the final line of Eq. (7). The free-term coefficient tensors can be rapidly computed for the entire surface using the FFT as will be described in Section 4.3, avoiding the $O(N^2)$ operational expense for computing these same terms directly.

The analogous form for the weakly singular stress-BIE is,

$$\begin{aligned}
0 &= -\int_{S_L} [u_i(\mathbf{Q}) - u_i^L(\mathbf{P},\mathbf{Q})]V_{kijl}(\mathbf{P},\mathbf{Q})n_j(\mathbf{Q})\,\mathrm{d}S(\mathbf{Q}) \\
&\quad - \int_{S_L} [t_i(\mathbf{Q}) - \sigma_{im}(\mathbf{P})n_m(\mathbf{Q})]\tilde{\sigma}_{ikl}(\mathbf{P},\mathbf{Q})\,\mathrm{d}S(\mathbf{Q}) \\
&\quad - \int_{S-S_L} u_i(\mathbf{Q})V_{kijl}(\mathbf{P},\mathbf{Q})n_j(\mathbf{Q})\,\mathrm{d}S(\mathbf{Q}) \\
&\quad - \int_{S-S_L} t_i(\mathbf{Q})\tilde{\sigma}_{ikl}(\mathbf{P},\mathbf{Q})\,\mathrm{d}S(\mathbf{Q}) \\
&\quad + u_i(\mathbf{P})\int_{S-S_L} V_{kijl}(\mathbf{P},\mathbf{Q})n_j(\mathbf{Q})\,\mathrm{d}S(\mathbf{Q}) \\
&\quad + u_{i,m}(\mathbf{P})\int_{S-S_L} [x_m(\mathbf{Q}) \\
&\quad - x_m(\mathbf{P})]V_{kijl}(\mathbf{P},\mathbf{Q})n_j(\mathbf{Q})\,\mathrm{d}S(\mathbf{Q}) \\
&\quad + \sigma_{im}(\mathbf{P})\int_{S-S_L} n_m(\mathbf{Q})\tilde{\sigma}_{ikl}(\mathbf{P},\mathbf{Q})\,\mathrm{d}S(\mathbf{Q}) \\
&= -\int_{S_L} [u_i(\mathbf{Q}) - u_i^L(\mathbf{P},\mathbf{Q})]V_{kijl}(\mathbf{P},\mathbf{Q})n_j(\mathbf{Q})\,\mathrm{d}S(\mathbf{Q}) \\
&\quad - \int_{S_L} [t_i(\mathbf{Q}) - \sigma_{im}(\mathbf{P})n_m(\mathbf{Q})]\tilde{\sigma}_{ikl}(\mathbf{P},\mathbf{Q})\,\mathrm{d}S(\mathbf{Q}) \\
&\quad - \int_{S-S_L} u_i(\mathbf{Q})V_{kijl}(\mathbf{P},\mathbf{Q})n_j(\mathbf{Q})\,\mathrm{d}S(\mathbf{Q}) \\
&\quad - \int_{S-S_L} t_i(\mathbf{Q})\tilde{\sigma}_{ikl}(\mathbf{P},\mathbf{Q})\,\mathrm{d}S(\mathbf{Q}) + u_i(\mathbf{P})F\mathrm{IV}_{kil} \\
&\quad + u_{i,m}(\mathbf{P})F\mathrm{V}_{mkil} + \sigma_{im}(\mathbf{P})F\mathrm{VI}_{mikl} \quad (8)
\end{aligned}$$

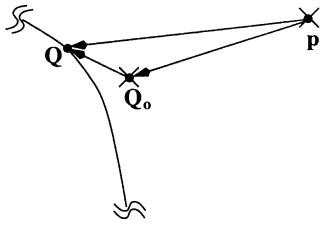

Fig. 1. Multipole expansion point $\mathbf{Q}_0$ for a surface element with the source point located at $\mathbf{p}$.

One of the redundant indices in the stress-BIE is removed through multiplication with the surface normal at $\mathbf{P}$ as is typically done to produce a traction-BIE.

$$0 = [\sigma_{kl}^{\mathrm{LC}}(\mathbf{P}) + \sigma_{kl}^{\mathrm{RI}}(\mathbf{P}) + u_i(\mathbf{P})F\mathrm{IV}_{kil} + u_{i,m}(\mathbf{P})F\mathrm{V}_{mkil} + \sigma_{im}(\mathbf{P})F\mathrm{VI}_{mikl}]n_k(\mathbf{P}). \tag{9}$$

Eqs. (7) and (9) are the bases for the present spectral multipole BEM algorithm depending on which form of the BIE is chosen for the solution. A general description of the computational treatment for each of the three types of terms in Eqs. (7) and (9) is given in Section 4 following a description of the multipole discretization in the next section.

3. Multipole representation of integral identities

In the present algorithm, only remote influences are conveyed through the multipole grid so the interior integral identities, Eqs. (1) and (2), can serve as a paradigm for the calculation of all remote integrals. The objective is to use the FFT as previously suggested [8,14,17] to avoid the computational expenses associated with computing a dense system matrix as well as subsequent matrix-vector multiplications as part of an iterative solution. The use of a uniform multipole grid to express integrals in the spectral BEM follows a previous algorithm [14]. Since multipole algorithms have certain nuances which differ from more traditional BEM algorithms, a brief description of the method follows in the remainder of this section and in the following section.

As is typically done in multipole schemes, a point $\mathbf{Q}_0$ which need not be part of any surface element is used to convey the influence of one or more surface elements in the system of equations as shown in Fig. 1. The kernels in the Somigliana identities are functions of the vector $\vec{r}(\mathbf{p},\mathbf{Q})$ which can be expanded in the following way.

$$\vec{r}(\mathbf{Q}-\mathbf{p}) = \vec{r}[(\mathbf{Q}_0-\mathbf{p}) + (\mathbf{Q}-\mathbf{Q}_0)]. \tag{10}$$

Expressing the vector $\vec{r}(\mathbf{p},\mathbf{Q})$ in the expanded form allows any general kernel function $K(\vec{r})$ to be written as follows for $\mathbf{Q}_0$ inside some radius of convergence.

$$\begin{aligned} K(\mathbf{Q}-\mathbf{p}) &= K[(\mathbf{Q}_0-\mathbf{p}) + (\mathbf{Q}-\mathbf{Q}_0)] \\ &= K(\mathbf{Q}_0-\mathbf{p}) + [\mathbf{Q}_j-\mathbf{Q}_{0j}]\,K_{,j}(\mathbf{Q}_0-\mathbf{p}) \\ &\quad + \tfrac{1}{2}[\mathbf{Q}_j-\mathbf{Q}_{0j}][\mathbf{Q}_k-\mathbf{Q}_{0k}]K_{,jk}(\mathbf{Q}_0-\mathbf{p}) + \cdots \end{aligned} \tag{11}$$

The surface bounding the domain may be broken into $\mathscr{M}$ elements and each element may be allowed to have a different point for the Taylor series expansion $\mathbf{Q}_{0M}$. For suitable choices of $\mathbf{Q}_{0M}$ inside a radius of convergence, the Somigliana identities may be expressed in the following forms.

$$\begin{aligned} u_l(\mathbf{p}) = \sum_{M=1}^{\mathscr{M}} \Bigg[& -\tilde{\sigma}_{lij}(\mathbf{p},\mathbf{Q}_{0M}) \int_{S_M} u_i(\mathbf{Q}) n_j(\mathbf{Q})\, \mathrm{d}S(\mathbf{Q}) \\ & + U_{li}(\mathbf{p},\mathbf{Q}_{0M}) \int_{S_M} t_i(\mathbf{Q})\, \mathrm{d}S(\mathbf{Q}) \\ & - \tilde{\sigma}_{lij,k}(\mathbf{p},\mathbf{Q}_{0M}) \int_{S_M} [x_k(\mathbf{Q}) \\ & - x_k(\mathbf{Q}_{0M})] u_i(\mathbf{Q}) n_j(\mathbf{Q})\, \mathrm{d}S(\mathbf{Q}) \\ & + U_{li,k}(\mathbf{p},\mathbf{Q}_{0M}) \int_{S_M} [x_k(\mathbf{Q}) - x_k(\mathbf{Q}_{0M})] t_i(\mathbf{Q})\, \mathrm{d}S(\mathbf{Q}) \\ & - \frac{1}{2}\tilde{\sigma}_{lij,km}(\mathbf{p},\mathbf{Q}_{0M}) \int_{S_M} [x_k(\mathbf{Q}) - x_k(\mathbf{Q}_{0M})][x_m(\mathbf{Q}) \\ & - x_m(\mathbf{Q}_{0M})] u_i(\mathbf{Q}) n_j(\mathbf{Q})\, \mathrm{d}S(\mathbf{Q}) \\ & + \frac{1}{2} U_{li,km}(\mathbf{p},\mathbf{Q}_{0M}) \int_{S_M} [x_k(\mathbf{Q}) - x_k(\mathbf{Q}_{0M})][x_m(\mathbf{Q}) \\ & - x_m(\mathbf{Q}_{0M})] t_i(\mathbf{Q})\, \mathrm{d}S(\mathbf{Q}) + \cdots \Bigg] \end{aligned} \tag{12}$$

$$\begin{aligned} \sigma_{kl}(\mathbf{p}) = \sum_{M=1}^{\mathscr{M}} \Bigg[& -V_{kijl}(\mathbf{p},\mathbf{Q}_{0M}) \int_{S_M} u_i(\mathbf{Q}) n_j(\mathbf{Q})\, \mathrm{d}S(\mathbf{Q}) \\ & - \tilde{\sigma}_{ikl}(\mathbf{p},\mathbf{Q}_{0M}) \int_{S_M} t_i(\mathbf{Q})\, \mathrm{d}S(\mathbf{Q}) \\ & - V_{kijl,m}(\mathbf{p},\mathbf{Q}_{0M}) \int_{S_M} [x_m(\mathbf{Q}) \\ & - x_m(\mathbf{Q}_{0M})] u_i(\mathbf{Q}) n_j(\mathbf{Q})\, \mathrm{d}S(\mathbf{Q}) \\ & - \tilde{\sigma}_{ikl,m}(\mathbf{p},\mathbf{Q}_{0M}) \int_{S_M} [x_m(\mathbf{Q}) \\ & - x_m(\mathbf{Q}_{0M})] t_i(\mathbf{Q})\, \mathrm{d}S(\mathbf{Q}) \\ & - \frac{1}{2} V_{kijl,mn}(\mathbf{p},\mathbf{Q}_{0M}) \int_{S_M} [x_m(\mathbf{Q}) - x_m(\mathbf{Q}_{0M})] \\ & \times [x_n(\mathbf{Q}) - x_n(\mathbf{Q}_{0M})] u_i(\mathbf{Q}) n_j(\mathbf{Q})\, \mathrm{d}S(\mathbf{Q}) \\ & - \frac{1}{2}\tilde{\sigma}_{ikl,mn}(\mathbf{p},\mathbf{Q}_{0M}) \int_{S_M} [x_m(\mathbf{Q}) - x_m(\mathbf{Q}_{0M})] \\ & \times [x_n(\mathbf{Q}) - x_n(\mathbf{Q}_{0M})] t_i(\mathbf{Q})\, \mathrm{d}S(\mathbf{Q}) + \cdots \Bigg] \end{aligned} \tag{13}$$

Restriction of the index M in the previous equations to points which lie in the far field allows the remote influence contributions in Eqs. (7) and (9) to be expressed in similar form. This is accomplished through grid blanking as described in Section 4.2.

By relating each density moment to its multipole expansion point $\mathbf{Q}_0$ the remote influences can be expressed as a sum over all the multipole expansion points,

$$u_l(\mathbf{p}) = \sum_{\mathbf{Q}_o=1}^{N_{\mathbf{Q}_0}} \Big[- \tilde{\sigma}_{lij}(\mathbf{Q}_0 - \mathbf{p}) D^u_{ij}(\mathbf{Q}_0) + U_{li}(\mathbf{Q}_0 - \mathbf{p}) D^t_i(\mathbf{Q}_0) - \tilde{\sigma}_{lij,k}(\mathbf{Q}_0 - \mathbf{p}) D^u_{kij}(\mathbf{Q}_0) + U_{li,k}(\mathbf{Q}_0 - \mathbf{p}) D^t_{ki}(\mathbf{Q}_0) + \cdots \Big], \tag{14}$$

$$\sigma_{kl}(\mathbf{p}) = \sum_{\mathbf{Q}_0=1}^{N_{\mathbf{Q}_0}} \Big[- V_{kijl}(\mathbf{Q}_0 - \mathbf{p}) D^u_{ij}(\mathbf{Q}_0) - \tilde{\sigma}_{ikl}(\mathbf{Q}_0 - \mathbf{p}) D^t_i(\mathbf{Q}_0) - V_{kijl,m}(\mathbf{Q}_0 - \mathbf{p}) D^u_{mij}(\mathbf{Q}_0) - \tilde{\sigma}_{ikl,m}(\mathbf{Q}_0 - \mathbf{p}) D^t_{mi}(\mathbf{Q}_0) + \cdots \Big], \tag{15}$$

where the density moments of various order for displacements and tractions have been written as D^u and D^t, respectively. When the multipole expansion points are organized as a regular grid, the resultant two-dimensional correlation sum can be rapidly computed by multiplication in the frequency domain with the FFT [14]. The use of the FFT and a regular grid can also be used as a post-processor for BEM solutions to provide various contour plots from the interior identities.

4. Direct spectral multipole BEM algorithm

Essential features of spectral multipole algorithms which use the FFT to convey remote influences include a blanking method to remove local influences from the grid data, an interpolation algorithm to express the remote influences at points not on the grid and an iterative solver for the resultant system of equations. Additionally, the grid data needs to be sampled in such a way so that the remote influences are suitable for evaluation as a Fourier correlation sum. The following sections describe how each of the three types of terms in Eqs. (7) and (9) are computed along with a description of the blanking that establishes whether elemental influences are calculated directly or through the multipole grid.

It is recognized [11,12] that iterative solvers do not perform as well on systems resulting from direct BEM applications as they do on systems arising from indirect methods [8,14]. Following a thorough study of iterative BEM solution techniques [1], the algorithm GMRES [28,29] has been chosen to solve the systems resulting from Eqs. (7) and (9).

4.1. Discretization and near field elements

In the present algorithm, the standard isoparametric representation is used with Lagrangian interpolation.

$$x_k(\xi) \approx \sum_{i=1}^{5} N_i(\xi) x^i_k, \tag{16}$$

$$u_k(\xi) \approx \sum_{i=1}^{5} N_i(\xi) u^i_k,$$

$$t_k(\xi) \approx \sum_{i=1}^{5} N_i(\xi) t^i_k.$$

The summations extend over five nodal values for the quartic shape functions used,

$$N_i(\xi) = \prod_{j=1}^{5} \frac{\xi - \xi_j}{\xi_i - \xi_j}, \qquad j \neq i. \tag{17}$$

Previous experience with an $O(r^2)$ stress-BEM has shown that quartic interpolations are required to yield comparable accuracy with other BEM algorithms using comparable degrees of freedom. It has been postulated [27] that the interpolation refinement which is necessary for whole-body regularized algorithms stems from the fact that integrals involving $O(r^2)$ density functions require a much better fit of the boundary data than integrals involving $O(1)$ density functions. Since the BEM system is typically dense, there appears to be little computational penalty for using high order elements [30] unlike in the finite element method where their use leads to an increase in bandwidth. An additional attractive feature of the quartic elements is that the derived quantities, stress and strain, which involve derivatives of the shape functions, are nearly as accurate as the boundary displacements and tractions [27].

The first terms in Eqs. (7) and (9) are the local contribution integrals. Since the near field integrals could be described as the conventional portion of the algorithm, the computational treatment of these terms is straightforward. All near field integrals in the reported examples are directly computed with Gaussian integration. The relaxed regularization [31,32] is used at nodes shared between two elements to remove all unbounded terms in the weakly singular stress-BIE. The relaxed regularization is also employed in the weakly singular displacement-BIE, though its use is a matter of convenience rather than one of necessity due to the reduced continuity requirement in the displacement-BIE. Further discussion of the regularizing states is given in Section 4.3. Direct integration over some fraction of the elements for each collocation point leads to a sparse coefficient matrix which is stored in compressed form.

When possible, the local contributions to the effective

system diagonal are used to precondition the system. The influences of the free terms described in Section 4.3 would also contribute to the diagonal in conventional BEM algorithms so that the method is not the usual point Jacobi preconditioning. It should also be noted that the strongly singular kernel corresponding to the fundamental stress exhibits antisymmetry with compressive stresses in front of the point load and tensile stresses behind the point load. In the instance that all of the near field elements are flat and aligned with one of the coordinate axes, the local weakly singular integrals involving the fundamental stress in Eqs. (7) and (9) may be zero or zero to within a small roundoff error. Similar algorithms should make provisions in such cases to use an alternate form for the relevant term in the preconditioner. In the present algorithm, the relevant term on the diagonal of the preconditioner is taken as unity in the instances when the local contribution to the linear system is nearly zero.

4.2. Remote influences

The second terms in Eqs. (7) and (9) are the remote influences which, for large systems, comprise the majority of the computational effort. Fig. 2 illustrates the multipole sampling scheme for a model problem which will later be taken as the first numerical example. A 32×32 multipole grid is used with a 3×3 blanking area. The algorithm centers the kernel source point sampling patch on the grid point located at the position $(N_x/2 + 1, N_y/2 + 1)$ as shown.

For grid-based FSM's arising from singular integral equations, the near field influences conveyed through the grid are grossly inaccurate. For schemes in which the near field contributions can be expressed in closed form in terms of finite quantities, some pre-corrections may be made to the grid data to remove the inaccurate near field influences [8]. However, due to the algebraic complexity of the local mapping of the density moment data to the grid for the present approach and the fact that the kernel functions are not finite at the source point on the grid, the strategy which has been chosen is the kernel blanking scheme [14] which insures that local influences are never part of the grid summations. Inside the blanking region indicated by the square of unfilled circles shown in Fig. 2 the kernel data are not computed, but rather, are set to zero.

Elemental grid point associations which are based on proximity to the element centroids determine, for each collocation point, whether the influence of each non-local element is computed directly or through the multipole grid. Another key association in the algorithm is established between each collocation point $\mathbf{P}$ and its closest grid point $\mathbf{G}^{\mathbf{P}}$. Those elements which have a closest grid point $\mathbf{Q}_0$ lying inside the blanking region centered at $\mathbf{G}^{\mathbf{P}}$ for the given node are blanked out of the correlation sums in Eqs. (14) and (15) since the corresponding kernel entries are set to zero. The direct local influences described in the previous section for each node $\mathbf{P}$ are the integrals over all elements having closest grid points $\mathbf{Q}_0$ which lie inside the blanking region centered at $\mathbf{G}^{\mathrm{P}}$.

The sampling of the kernel data and density moments in the manner described allows the elemental summations to be rapidly computed as Fourier correlation sums [33]. In the present notation, the kernels are written as functions of $\mathbf{Q}_0 - \mathbf{p}$ and the density moments are written as functions of $\mathbf{Q}_0$. Introducing a new variable, $\mathbf{T} = \mathbf{Q}_0 - \mathbf{p}$, the remote sums in Eqs.(14) and (15) take the forms,

$$u_l(\mathbf{p}) = \sum_{\mathbf{Q}_{ox}=1}^{N_x} \sum_{\mathbf{Q}_{oy}=1}^{N_y} \Big[- \tilde{\sigma}_{lij}(\mathbf{T}) D^u_{ij}(\mathbf{T} + \mathbf{p}) + U_{li}(\mathbf{T}) D^t_i(\mathbf{T} + \mathbf{p}) - \tilde{\sigma}_{lij,k}(\mathbf{T}) D^u_{kij}(\mathbf{T} + \mathbf{p}) + \cdots \Big], \quad (18)$$

$$\sigma_{kl}(\mathbf{p}) = \sum_{\mathbf{Q}_{ox}=1}^{N_x} \sum_{\mathbf{Q}_{oy}=1}^{N_y} \Big[- V_{kijl}(\mathbf{T}) D^u_{ij}(\mathbf{T} + \mathbf{p}) - \tilde{\sigma}_{ikl}(\mathbf{T}) D^t_i(\mathbf{T} + \mathbf{p}) - V_{kijl,m}(\mathbf{T}) D^u_{mij}(\mathbf{T} + \mathbf{p}) + \cdots \Big], \quad (19)$$

where the summation over the points $\mathbf{Q}_0$ has been expressed as a double sum over the rows and columns of all multipole grid points.

For any general data set $u(m, n)$ sampled on a uniform grid, its discrete Fourier transform [33] is given by the following.

$$DFT[u(m,n)] = \mathscr{U}(r,s) = \frac{1}{N_x N_y} \sum_{m=0}^{N_x - 1} \sum_{n=0}^{N_y - 1} u(m,n) \mathrm{e}^{(-2\pi i r m / N_x)} \mathrm{e}^{(-2\pi i s n / N_y)}. \quad (20)$$

As previously noted [14], the correlation sums in Eqs. (18) and (19) can be rapidly computed with the discrete transform using the correlation property,

$$DFT[u(m,n)] = DFT\left[\sum_{m=0}^{N_x - 1} \sum_{n=0}^{N_y - 1} \mathscr{K}(r,s) \mathscr{D}\mathscr{M}(m + r, n + s) \right] = \mathscr{K}(r,s) \mathscr{D}\mathscr{M}^*(r,s), \quad (21)$$

where $\mathscr{K}(r, s)$ is the transform of the general kernel function and $\mathscr{D}\mathscr{M}^*(r, s)$ is the complex conjugate of the transform of the general density moment. The FFT algorithm [34] can be used so that the total operation count required to transform the data, compute the correlation, and invert the result is $O(N_x N_y \log|N_x N_y|)$. For BEM models of highly porous media, the product $N_x N_y$ would be proportional to the number of elements. The operational expense of the matrix-vector multiplication is $O(N \log N)$ where N is the system size. As part of an iterative process, transformation of the kernel functions is only performed once so that the remaining operations only involve updates to the density moments.

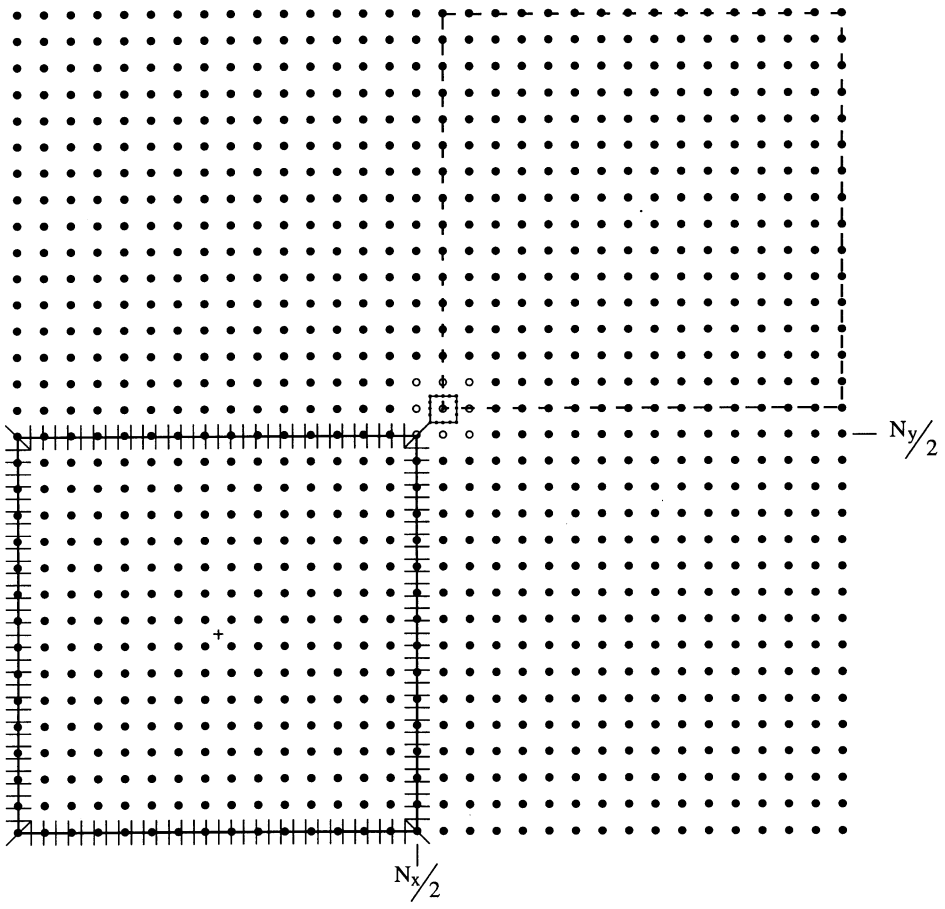

Fig. 2. 32×32 multipole grid representation of the Kirsch problem with blanking set at 3×3.

As seen in Fig. 2, the kernel functions are sampled at the grid points (r, s) corresponding to the point $\mathbf{T} = \mathbf{Q} - \mathbf{p}$ with the source points placed near the center of the grid. The density moments at $(m + r, n + s)$ are sampled as shown by the dashed region outlined in the upper right portion of the grid. The data are structured so that the correlation influence at the (m, n) position corresponding to the point $\mathbf{p}$ is in the physical location shown in the lower left of the grid. The physical domain occupies the lower left $(N_{x/2}) \times (N_{y/2})$ portion of the grid and the sampling location for density moments falls in the upper $(N_{x/2}) \times (N_{y/2})$ portion of the grid.

At internal grid points far from any boundary, the grid data naturally show the same variation with position as the interior solutions since the remote influences are the BEM approximations for internal stresses and displacements. For grid points which are close enough to the boundary so that the blanking region intersects the boundary, spatial variation in the remote influences is also significant. The quartic serendipity patch element [35] is used to resolve spatial variation in the remote influences. The remote influences at the collocation points which are not typically on the regular grid are approximated with the standard forms.

$$u_k^{\mathrm{RI}}(\vec{x}) \approx \sum_{i=1}^{17} N_i(\xi, \zeta)(u_k^{\mathrm{RI}})^i, \tag{22}$$

$$\sigma_{kl}^{\mathrm{RI}}(\vec{x}) \approx \sum_{i=1}^{17} N_i(\xi, \zeta)(\sigma_{kl}^{\mathrm{RI}})^i. \tag{23}$$

The translationally invariant kernel functions are sampled over the unblanked portions of the grid with the source point placed at each of the nodal positions on the serendipity patch element shown in Fig. 3. Computing the correlation with each translation of the kernel data gives the nodal values used in the interpolation, $(u_k^{\mathrm{RI}})^i$ and $(\sigma_{kl}^{\mathrm{RI}})^i$. The width of the interpolation patch is equal to the grid spacing and the patch boundaries lie halfway between adjacent grid points. The coordinates of the collocation node relative to its closest grid point $x_i^{\mathbf{P}} - x_i^{\mathbf{G^P}}$ are mapped to the intrinsic coordinates (ξ, ζ) on the serendipity patch.

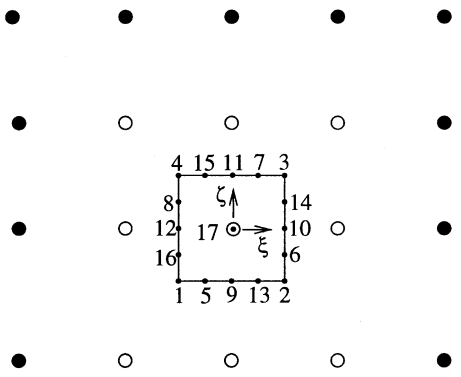

Fig. 3. Serendipity kernel patch element near the center of the multipole grid.

4.3. Regularizing boundary data

The final type of terms which need to be evaluated for the regularized multipole algorithm are comprised of products of the boundary data and integrals of various kernel functions over the non-local elements. The regularizing states require an expression for displacement gradients in terms of the BEM interpolations for boundary displacements and tractions. The BEM approximation for displacement gradients follows from the tangential derivatives of the displacements, the surface form of Hooke's law, and the strain-displacement relations. Tractions are related to displacement gradients through,

$$t_j = \frac{2\mu\nu}{1-2\nu} u_{m,m}\delta_{ij}n_i + \mu(u_{i,j} + u_{j,i})n_i \tag{24}$$

and surface tangential derivatives of the displacement are related to the displacement gradients through,

$$\sum_{i=1}^{5} N_i'(\xi)u_j^i = -Jn_2u_{j,1} + Jn_1u_{j,2}, \tag{25}$$

where $N_i'(\xi)$ represents the derivatives of the interpolation function with respect to the intrinsic coordinate, J is the Jacobian of the transformation to the standard element, n_i are the components of the surface normal vector, and μ and ν are the shear modulus and Poisson's ratio, respectively. Though the expression in Eq. (25) is a two-dimensional result, the analogous result for three-dimensional problems simply follows from application of the chain rule of partial differentiation.

Through inversion of the relations in Eqs. (24) and (25), the displacement gradients in the BEM take the following form:

$$u_{k,l}(\mathbf{P}) \approx A_{klm}(\xi^{\mathbf{P}})t_m(\xi^{\mathbf{P}}) + B_{klm}(\xi^{\mathbf{P}})\sum_{i=1}^{5} N_i'(\xi^{\mathbf{P}})u_m^i. \tag{26}$$

In the previous expression, $\xi^{\mathbf{P}}$ is the intrinsic coordinate at $\mathbf{P}$, $t_m(\xi^{\mathbf{P}})$ is the traction at the source point, u_m^i are the nodal values of displacement and the elemental summation extends over the five nodes in the two-dimensional quartic element. The terms in the tensors A_{klm} and B_{klm} involve the elastic constants, the surface normal vector and the Jacobian. The BEM estimate for stresses is formed from the displacement gradients using Hooke's law and the strain-displacement relations. Following the standard relaxed regularization approach [36,37], the regularizing state on each source point element is given in terms of the interpolation on that element. In the case that the source point is shared between elements, the value of the regularizing state in the far field is taken as an elemental average [25,27].

The integrals $F\mathrm{I}_{li}$ and $F\mathrm{III}_{mli}$ which multiply the free-term displacement and stress, respectively, in Eq. (7), involve products of the kernels $\tilde{\sigma}_{lij}$ and U_{li} and the normal vectors. The forms for $F\mathrm{I}_{li}$ and $F\mathrm{III}_{mli}$ are easily obtained using the same computational architecture since the normal vector density moments are the standard displacement density moments for the particular case of unit displacements. By forming the appropriate correlation sums, the resulting free-term coefficients are rapidly computed for all nodes using the FFT. The same blanking method used to isolate the remote influences of the boundary data only on $S - S_L$ are used to similarly isolate the remote influences of the regularizing states on $S - S_L$. The analogous terms $F\mathrm{IV}_{kil}$ and $F\mathrm{VI}_{mikl}$ in Eq. (9) are treated in the same manner. Calculation of the displacement gradient free term coefficient tensors $F\mathrm{II}_{mli}$ and $F\mathrm{V}_{mkil}$ may also be performed with the multipole approximation. Taking the former as an example, the tensor can be written as follows.

$$\begin{aligned} F\mathrm{II}_{mli} &= \int_{S-S_L} [x_m(\mathbf{Q}) - x_m(\mathbf{P})]\tilde{\sigma}_{lij}(\mathbf{P},\mathbf{Q})n_j(\mathbf{Q})\,\mathrm{d}S(\mathbf{Q}) \\ &= \int_{S-S_L} \tilde{\sigma}_{lij}(\mathbf{P},\mathbf{Q})x_m(\mathbf{Q})n_j(\mathbf{Q})\,\mathrm{d}S(\mathbf{Q}) \\ &\quad - x_m(\mathbf{P})\int_{S-S_L} \tilde{\sigma}_{lij}(\mathbf{P},\mathbf{Q})n_j(\mathbf{Q})\,\mathrm{d}S(\mathbf{Q}). \end{aligned} \tag{27}$$

The first integral in the second line of the previous expression is easily computed as a correlation sum involving a constant strain density moment and the other integral is of the same form as $F\mathrm{I}_{li}$ multiplying the rigid-body term. The vector $x_m(\mathbf{P})$ which appears outside the second integral is included as part of the product with the displacement gradient after the remote influence at the source point is computed involving only $O(N)$ multiplications.

5. Numerical results

The computational savings which may be gained through multipole methods are well-documented [8,10,11,14,16]. Since multipole schemes are only practical for use with relatively large systems that require substantial computational effort, it is impractical to conduct numerical convergence studies for every simulation. This section will therefore include a discussion of the parameters required to obtain accurate BEM solutions as well as a report of

the computational savings obtained through the present algorithm.

In addition to the familiar errors associated with truncation of the Taylor series expansions, other sources of modeling error will coexist within the SMM. A small amount of error may result from the application of iterative solution methods to poorly conditioned systems. Another inherent source of error in the SMM will arise from interpolation of the remote influences. For a fixed grid and blanking, the remote interpolation error will place a limitation on the accuracy which can be obtained in the effective matrix-vector multiplication which will be independent of the multipole expansion order. Without refinement of the multipole grid, the remote interpolation error will also ultimately limit the increased solution accuracy which would otherwise be expected from BEM mesh refinement.

Due to the complex relationship between sources of error present in the SMM, a formal error analysis will not be attempted. Rather, the variables influencing solution accuracy will simply be reported as they are observed from numerical experimentation. A dimensionless parameter κ which may provide some indication for modeling error is defined as

$$\kappa = \frac{\sup|\mathbf{Q} - \mathbf{Q}_0|}{|r_b|}, \tag{28}$$

where the numerator represents the maximum distance between a Gauss point on any element and its elemental expansion point and r_b is half the width of the blanking square. It should be noted that for a fixed blanking radius, κ will decrease with grid refinement and that for a fixed grid, κ will also decrease for increased blanking so that smaller values of κ should correlate with increased accuracy.

For all examples, the unrestarted version of GMRES was used with the initial guess taken as the null vector. Following extensive numerical experimentation, no convergence criterion could be determined based on a unique value for the residual norm which would not lead to overly conservative estimates for at least some systems. For the SMM systems which were not too poorly conditioned, plots of the logarithm of the residual norm versus iteration number indicated the common tendency for the residual norm to decrease very rapidly through the early iterations and then to abruptly change to a slope which was nearly zero. Accurate solutions were not obtained when GMRES was stopped while the residual norm was still decreasing in the iterative process. Numerical experiments seemed to indicate that the best convergence measure was to stop GMRES just after the residual curve became flat for a number of iterations. A 3% decrease in the residual norm over 75 iterations was most often used as the convergence criterion so that execution did not terminate prematurely in the few instances in which the residual norm followed a staircase descent. Additionally, the preconditioners used for each example will be discussed in the remainder of this section as well as the scaling which seemed to be required for the second example.

5.1. Plate with hole subjected to remote tension

Motivation for the development of the present multipole algorithm is largely based on the need to simulate the evolution and coalescence of voids in porous media. The multipole solutions for a large plate with a small hole can be used to gain insight into the expected behavior for large scale simulations of porous elastic media.

Some background on the two conventional forms of the stress-BEM and displacement-BEM is first in order. A key difference between applying the two forms of the BEM stems from integration of the various kernels around closed surfaces. The integral of the hypersingular kernel around a closed surface such as a pore is known to be zero [38]. The displacement solution resulting from the stress-BEM applied to geometries containing internal closed surfaces on which there is no displacement boundary condition will be arbitrary to within a translation and rotation of the closed surface. When direct solvers are used for the system generated using the SSI, the displacement solution on the pore will include some non-physical rigid body terms. On the other hand, an iterative method such as GMRES which builds a Krylov sequence annihilates the null space so that the rigid body component of the solution on the pore will be zero to within some small round-off error. The clear indication that the iterative and direct solutions of the stress-BEM differ only by stress-free rigid body terms follows from the fact that the boundary stress algorithm, which requires differentiation of the displacement field, yields identical results for the two BEM solutions to within round-off error.

A second difference between the stress-BEM and the displacement-BEM is the integration order which is apparently necessary. As an example, the boundary stresses computed from applying the conventional forms of the BEM to the four element model of the pore shown in Fig. 4 will be compared. It should be noted that the requirement for accurate boundary stresses is more stringent than the usual requirement for accurate nodal boundary data since stresses are computed from differentiation of the shape functions. From the preceding discussion, however, a comparison of boundary displacements around the pore is meaningless. Using the conventional stress-BEM with eighth-order integration, the extreme stress concentration factors differ from the exact results [39] of 3 and -1 by only 0.056% and 0.54%, respectively. The small errors remain unchanged to at least four significant figures when the integration is refined from eighth-order to twelfth-order. The conventional displacement-BEM, however, shows a significant improvement under refinement from tenth-order to twelfth-order integration as errors in the same quantities are reduced from 2.8% and 4.0% to -0.91% and -0.21%, respectively. The fact that the weakly singular displacement-BIE contains integrands which are very

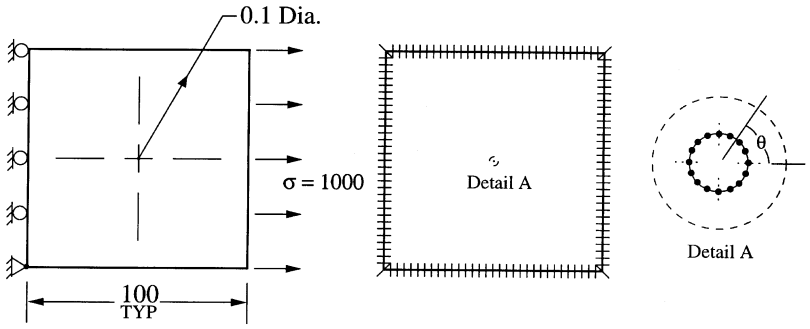

Fig. 4. Plate with hole in tension and 132 quartic element BEM model.

small over a larger region seems likely to explain the requirement for higher order integration in the displacement-BEM. The examples to be presented were therefore solved using eighth-order integration in the stress-BEM and twelfth-order integration in the displacement-BEM.

With the conventional BEM solutions for the small hole subjected to remote tension as a baseline, the 32×32 multipole grid previously shown in Fig. 2 was used for the SMM solutions for the problem. As shown, the blanking region for both forms of the SMM was a 3×3 array of gridpoints. The choice to place 128 elements around the periphery of the plate as shown in Fig. 4 was made to provide a level of discretization suitable for application of the SMM. The numerical value for the Young's modulus was taken as 3×10^7 and 0.3 was used for the Poisson's ratio. For both the displacement-BEM and stress-BEM, the kernel expansions were carried out through third order derivatives. Kernel truncation after second order derivatives led to an error in the system which produced traction errors at the corners of the plate which were around 3% though the remainder of the traction solution was still highly accurate.

The stress concentration factors from the SMM are shown in Fig. 5 where the boundary stress was computed from the surface form of Hooke's law and then rotated into the cylindrical system. The choice to compute stresses only at the nodal positions was arbitrary; the quartic elements support a highly accurate estimate for stresses at all points on the element. As seen in Fig. 5, a single quartic element spanning each arc of $\pi/2$ as shown in the detail drawing of Fig. 4 was sufficient to accurately model the stress variation along the pore. For this problem, the influence of the remote loading was conveyed to the nodes on the pore exclusively through the multipole grid. The errors in the SMM stress-BEM for the stress concentration factors at $\pi/2$ and 0 were 0.042% and 0.53% while for the SMM displacement-BEM, the same errors were -0.95% and -0.27%. By comparison with the conventional BEM solutions previously described, errors due to the SMM approximation were slightly less for the stress-BEM. In both SMM solutions, the tractions computed on the left were equal to the applied tractions to at least six significant figures at all places including the corners. The small difference between the applied and computed tractions is expected due to the presence of the hole in the finite geometry.

A test for the level of accuracy which can be expected from truncation after third order derivatives was conducted using the SMM stress-BEM by removing the hole from the plate. The stress-BEM patch test for the third order SMM showed that the computed tractions were equal to the applied tractions to at least ten significant figures using the same grid and blanking scheme.

The nodal displacements should now be interpreted in light of the previous discussion regarding closed surfaces. The displacements from the SMM displacement-BEM along the horizontal and vertical centerlines of the pore matched the corresponding mid-side plate displacements to within a small error in the seventh significant figure along the vertical center line and to eight significant figures along the horizontal centerline. From the SMM stress-BEM, the same displacements on the centerlines of the pore were more than six orders of magnitude smaller than the corresponding mid-side plate displacements as expected in light of the previous discussion regarding GMRES and the null space in the stress-BEM system.

With the blanking used in this example, the number of elements placed in the far field for each collocation point ranged between 124 and 128, which is between 93.9% and

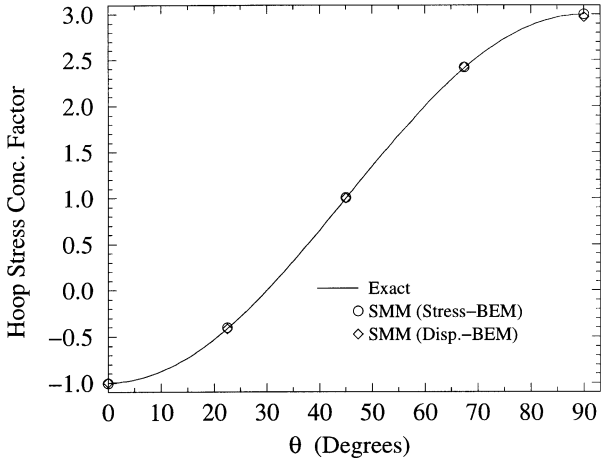

Fig. 5. Stress concentration around hole with blanking set at 3×3 and truncation after third order derivatives.

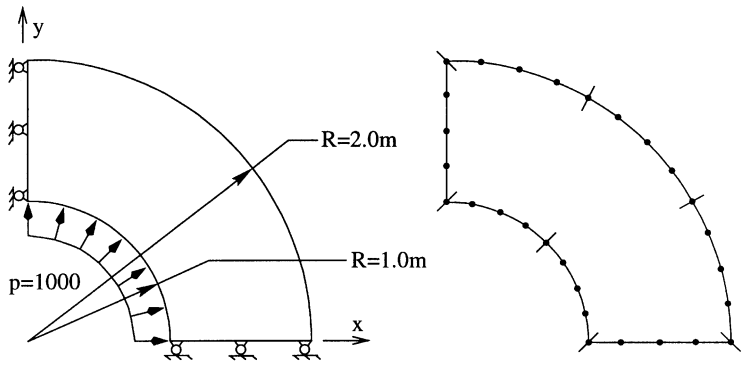

Fig. 6. Pipe subjected to internal pressure.

97.0% of the total elements in the model. The dimensionless κ factor for the 3×3 blanking used with this discretization was approximately 0.468.

5.2. Pressurized pipe

The second numerical example is a pipe subjected to internal pressure as shown in Fig. 6. BEM solutions for this problem are more interesting since the algorithm must compute tractions on surfaces which have significant stress gradients. As a reference, basic four element models of the pipe give maximum traction errors of 2.3% and 1.4%, respectively, for the conventional implementations of the stress-BEM and the displacement-BEM using quartic elements and eighth-order and twelfth-order integration, also respectively. However, seven elements were used in the initial discretization as shown in Fig. 6 because it seemed more convenient to assess blanking requirements in models with nearly uniform element sizes. Subsequent mesh refinements were performed by dividing each element shown in Fig. 6 in half.

For this problem, a 64×64 multipole grid was used as plotted in Fig. 7 where only the portion of the grid which contained the physical location of the pipe is shown. The plot shows a discretization with 224 elements with the nodes shared between elements plotted to provide a sense of the element size. The plot also shows the 5×5 blanking region which seemed to be best suited for this discretization. The units of the plot are shown in cm as will be explained.

The poor conditioning for BEM problems in elasticity is largely due to the fact that, for geometries which are $O(1)$ in size, the unknown tractions and displacements differ by the order of the elastic modulus. For straightforward boundary integral discretizations in elasticity, then, the columns of the system matrix are likely to be poorly scaled which adversely affects conditioning [40]. While the disparity in magnitude between the two types of boundary data never seems to pose any problem for direct solvers, the accuracy and efficiency of iterative solvers under these conditions is compromised. For the pressurized pipe example, the process of column scaling was employed and conditioning of the linear systems was observed to improve considerably. Since the SMM never explicitly builds a full system matrix, the equivalent process of column scaling was based on an appropriate choice of units taken from dimensional analysis. The following general scaling argument can be made,

$$u \sim \epsilon L \sim \frac{\sigma L}{E} \sim \frac{tL}{E} \tag{29}$$

where the omission of indices on the quantities u, t, σ and on the strain ϵ indicates characteristic values for the corresponding vector and tensor quantities and where E and L are the Young's modulus and the characteristic length, respectively. The scaling immediately gives the following pi group

$$\Pi_1 = \frac{tL}{Eu} \tag{30}$$

which should be an $O(1)$ term. If the conventional linear system was to be formed, it should be expected that the columns of the system matrix are nearly optimally scaled when the magnitudes of the unknown tractions and

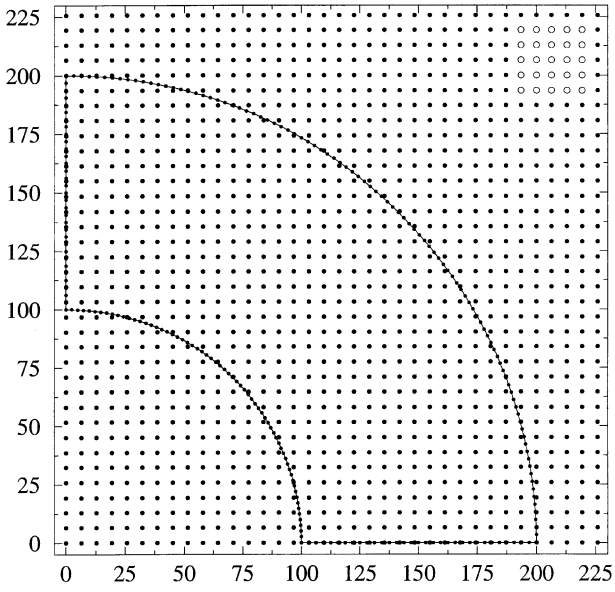

Fig. 7. A portion of the 64×64 multipole grid overlying a 224 element model of the pressurized pipe shown in its physical location.

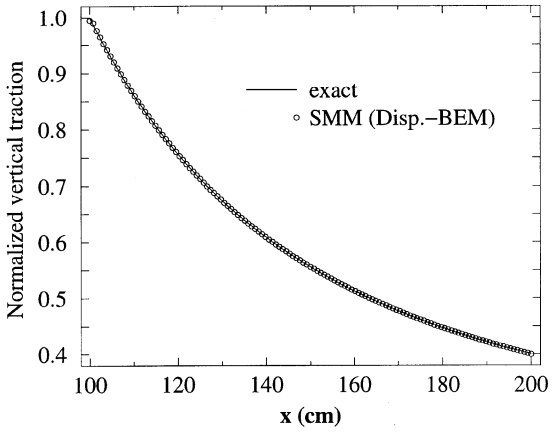

Fig. 8. Tractions from SMM displacement-BEM using 224 elements with 5×5 blanking and 64×64 grid.

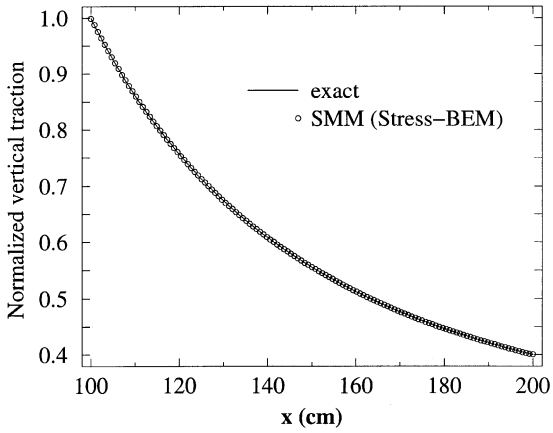

Fig. 9. Tractions from SMM stress-BEM using 224 elements with 5×5 blanking and 64×64 grid.

unknown displacements are nearly equal. Since Π_1 is $O(1)$, this will occur when the numerical value of the ratio L/E is close to unity.

As an example, two systems of units were used with the SMM models for the pressurized pipe. The outside diameter of the pipe which was 2 m served as the characteristic length for the problem. The pressure inside the pipe was taken to be 10^3 Pa and the Young's modulus for the pipe was taken as 3×10^7 Pa. In the standard SI system, the ratio of characteristic tractions to displacements was $O(10^7)$ corresponding to an L/E ratio of about 6.7×10^{-8}. Under rescaling in terms of cm, the ratio of characteristic tractions to displacements was reduced to $O(10)$ which corresponds to a more favorable L/E ratio of 6.7×10^{-2}.

The benefits from column scaling are summarized as follows. When the problem was formulated in the usual SI system, GMRES routinely gave errors of around 2% for the computed tractions at the corner nodes as computed from the stress-BEM, though the tractions computed at all other nodes were typically accurate to around four significant figures. Additionally, the number of iterations of GMRES was required to be as high as $0.9N$ for some models where N denotes the system size. By simply rescaling the problem as described, the errors in the tractions at the corners were reduced by at least an order of magnitude. Additionally, using the second system of units, the number of iterations was reduced to around $0.1N$ for the larger systems which was sufficient for the SMM to offer a computational advantage over the conventional BEM. It should be noted that rescaling of the problem changed the preconditioner which also may have contributed to the improvement seen in the stress-BEM.

In order to observe the accuracy of GMRES under the two scaling schemes without the approximations introduced by the SMM, a number of runs were made with modified dimension statements so that the entire grid was blanked out to recover the conventional linear systems. When the problem was rescaled in terms of cm for the basic unit of length, the solution vectors from GMRES matched the direct solutions in at least the first seven significant figures with or without preconditioning. When the problem was formulated in terms of m, GMRES was only able to consistently match the first four significant figures in the solution vector compared to the direct solution.

A final note on conditioning concerns the displacement-BEM. Using the inverse of the local contribution to the system diagonal as a preconditioner for the displacement-BEM failed as GMRES did not solve the system. Though the same preconditioner worked for the previous problem, the results in this section from the displacement-BEM were obtained without preconditioning.

The numerical results presented in the plots in this section were again obtained using third order expansions in the SMM. Third order expansions were chosen because errors were observed in the solutions obtained with truncation following the second order derivatives and the solution vectors were unchanged to four significant figures under successive refinements from third order through fifth order. An example of the tractions computed by the SMM displacement-BEM is shown in Fig. 8, where the tractions are normalized to the maximum value of traction in the exact solution [18]. As seen in Fig. 8 the SMM displacement-BEM produced a small traction error in the corner where $x = 100$ of about 0.56%. This was due to the *far field* approximation since the conventional displacement-BEM shows an error of only 0.025%. The remainder of the traction solution was extremely accurate. The tractions computed by the SMM stress-BEM were much more accurate as seen in Fig. 9 and show a maximum error of 0.17% which occurred at the corner where $x = 200$. Plots of the displacement solution are not given since the displacements were accurate everywhere to at least four significant figures.

The use of a 5×5 blanking region on the 64×64 grid produced values of κ which ranged from about 0.324 for the 224 element model to around 0.295 for the 896 element model. For the models ranging in size from 224 elements to 896 elements, the fraction of elements placed in the far

field at each collocation point by the 5×5 blanking was between 92% and 96%.

The limitation on the blanking level for this problem is illustrated by attempts to reduce the blanking to a 3×3 square. When the blanking was reduced to 3×3, the SMM stress-BEM produced traction errors at the corners which were on the order of 1–2% even though the expansions were carried out through fifth order derivatives. The corresponding κ factors for the 3×3 blanking runs were around 0.5. Therefore, the conservative blanking criterion observed for the pressurized pipe example is that κ should be equal to or less than 0.3.

The key motivation for the present work lies in the computational advantage which can be gained through the SMM for large systems. Benchmarking was performed on a Sun Microsystems HPC(Enterprise) 450 with 4 UltraSparc II 248MHz processors and 1GB of memory to compare run times for the conventional and SMM forms of the stress-BEM for the pressurized pipe examples. For the 224 element, 448 element and 896 element models, the conventional BEM gave maximum corner traction errors of 0.054%, 0.024%, and 0.011%, respectively. As should be expected due to the errors associated with interpolation of the remote influences which are fixed for a given grid, the SMM was not able to show a similar convergence trend nor maintain the same level of accuracy as the conventional BEM. However, among the same three models, the maximum corner traction error in the solutions obtained with the SMM was only 0.19% which should be acceptable in nearly any practical application. The run times for the two forms of the stress-BEM are plotted in Fig. 10. For the pressurized pipe example, the figure indicates a computational advantage for the SMM for BEM models which have more than about 400 quartic elements.

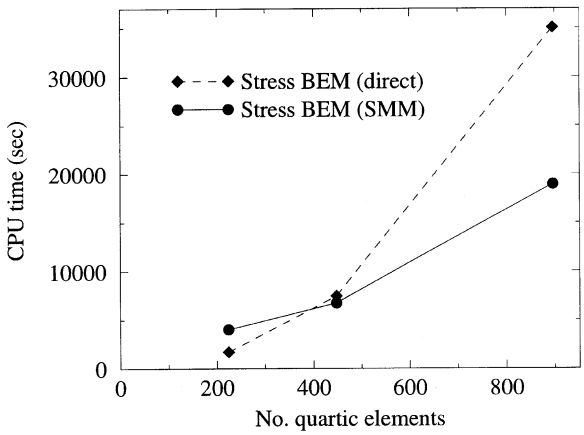

Fig. 10. Algorithm speed comparison with SMM solution errors maintained under 0.2%.

6. Conclusions

An implementation of the SMM was demonstrated for the weakly singular forms of the displacement-BIE [41] and the stress-BIE. Even for problems of moderate size, the SMM was shown to be faster than the conventional BEM while maintaining a level of accuracy suitable for engineering calculations. It should be noted that the computational advantage of the SMM was observed in the second example in spite of the heterogeneous spatial distribution of elements. Since it is recognized [8] that the efficiency of spectral grid-based methods is highest for element distributions which are nearly homogeneous in space, it should be expected that the computational advantage for the SMM would be even more pronounced for models of highly porous media.

A guideline for the appropriate blanking radius to establish whether elemental influences should be conveyed directly or through the multipole grid may be inferred from the minimum value of the κ ratio which was required in the two example problems. While accurate results were obtained in the first example with κ nearly as high as 0.5, a similar value of κ in the second example was associated with levels of error which would typically be considered as unacceptable. Therefore, the requirement from the second example that κ must be less than or about 0.3 should be taken as the more conservative estimate for the minimum blanking radius for a given grid and discretization. This is only slightly more conservative than the definition of well-separated sets described in early references to the use of multipoles [6]. The small difference is likely to be due to the fact that the SMM is additionally limited by errors in the interpolation of the remote influence grid data.

In each of the two example problems, second order expansions were found to be insufficient. It was also observed that the solution vectors were essentially unchanged under refinements beyond third order expansions which is consistent with the position that the primary limitation on accuracy in the SMM is the order of interpolation for the remote influences. Based on the reported examples, then, Taylor series truncation after the third order derivatives would seem to be preferred in terms of accuracy and computational expense.

Use of the SMM has provided some unexpected insight regarding BEM tractions at corner nodes. It is widely recognized that tractions at corners are extremely sensitive to small amounts of modeling errors in BEM systems. It should be noted that the SMM and the conventional BEM share the integrations in the near field which are sufficient to give traction solutions with errors which are always considerably less than 0.1% in the conventional BEM solutions of the example problems. Introducing non-local perturbations to the system of equations by truncating the kernels in the far field and interpolating remote influences was seen on many occasions to have a significant effect on the corner tractions while the remainder of the boundary solution was essentially unchanged. The implication is that, while tractions at corners seem to be an excellent indicator for overall system modeling error, this sensitivity has a strong non-local nature which is

attributable to factors other than the usual concerns regarding boundary integral equations for external corners.

Some possibilities for improvement to the algorithm should be suggested. First, a database for kernel tables could easily be developed where the entries are stored in the frequency domain. The data could be stored for kernels sampled on a grid of unit characteristic dimension. Dimensional analysis could be used to reproduce any kernel field on a geometrically similar grid of arbitrary size by scaling the kernel data from the basic table.

A second possible improvement might follow from iteratively solving an over-determined system of equations which would be too costly for conventional approaches. Using the form of the SMM described herein, the option to compute both the displacement-BIE and the stress-BIE for each collocation point is actually fairly inexpensive. The density moments are identical so that one set of transformed density moments is all that is required in the multipole expression for the two BIE's, the expensive matrix-vector multiplication is largely replaced with the FFT and a common kernel is shared between the two BIE's. The present algorithm which was successful in the benchmarking has not yet been optimized and computes all three kernel tables regardless of which form of the BEM is chosen. In addition to the computational advantages which might exist for rectangular iterative solvers, a heuristic based on mechanical arguments could be employed which uses both forms of the BIE so that updates to the unknown boundary data would be based on the error in the BIE expression for the known boundary data. The possibility for using such iterative solvers should be similarly considered for SMM applications to problems in potential theory.

A final suggestion became apparent through the post-processing of interior data when it was was noticed that the midside data from the serendipity nodes were continuous to machine precision. A more efficient approach would be to extend the multipole grid slightly so that the grid extends past the domain. With this approach, the kernels would only need to be sampled with the source point at the center node, at one corner node, and at the three interior nodes on one vertical and one horizontal side of the patch element. The expense for computing the remote influences both in terms of memory and in the number of required operations would be reduced to approximately 8/17 of the expense in the current algorithm while still providing a quartic interpolation by borrowing from the correlation influences in adjacent cells.

Acknowledgements

This research was supported in part by the Applied Mathematical Science Research Program of the Office of Mathematical, Information, and Computational Sciences, U.S. Department of Energy, under contract DE-AC05-00OR22725 with UT-Battelle, LLC. Additional support was provided by the Laboratory Directed Research and Development Program of the Oak Ridge National Laboratory. The first author would like to extend his sincere appreciation to C. Yang of ORNL for some very beneficial discussions regarding algorithms for linear systems.

References

[1] Kane JH, Keyes DE, Guru Prasad K. Iterative solution techniques in boundary element analysis. Int J Numer Meth Engng 1991;31:1511–36.

[2] Lachat LC, Watson JO. A second generation boundary integral program for three dimensional elastic analysis. In: Cruse TA, Rizzo FJ, editors. Boundary-integral equation method: computational applications in applied mechanics, vol. 11. New York: ASME, 1975 (AMD).

[3] Lachat LC, Watson JO. Progress in the use of boundary integral equations, illustrated by examples. Comput Meth Appl Mech Engng 1977;10:273–89.

[4] Kamiya N, Iwase H, Kita E. Parallel implementation of boundary element method with domain decomposition. Engng Anal Boundary Elem 1996;18:209–16.

[5] Fu Y, Overfelt JR, Rodin GJ. Fast summation methods and integral equations. In: Bonnet M, Sändig A-M, Wendland WL, editors. Mathematical aspects of boundary element methods. London: Chapman & Hall/CRC, 2000. p. 128–39.

[6] Greengard LF. The rapid evaluation of potential fields in particle systems. Cambridge, MA, USA: MIT Press, 1988.

[7] Barnes J, Hut P. A hierarchial $O(N \log N)$ force-calculation algorithm. Nature 1986;324:446–9.

[8] Phillips JR, White JK. A precorrected-FFT method for electrostatic analysis of complicated 3-D structures. IEEE Trans Computer-Aided Des Int Circuits Systems 1997;16(10):1059–72.

[9] Rokhlin V. Rapid solution of integral equations of classical potential theory. J Comput Phys 1985;60:187–207.

[10] Greengard L, Rokhlin V. A fast algorithm for particle simulations. J Comput Phys 1987;73:325–48.

[11] Gómez JE, Power H. A multipole direct and indirect BEM for 2D cavity flow at low Reynolds number. Engng Anal Boundary Elem 1997;19:17–31.

[12] Mammoli AA, Ingber MS. Stokes flow around cylinders in a bounded two-dimensional domain using multipole-accelerated boundary element methods. Int J Numer Meth Engng 1999;44(7):897–917.

[13] Greengard L, Moura M. On the numerical evaluation of elastostatic fields in composite materials. Acta Numer 1994:379–410.

[14] Peirce AP, Napier JAL. A spectral multipole method for efficient solution of large-scale boundary element models in elastostatics. Int J Numer Meth Engng 1995;38:4009–34.

[15] Greengard L, Rokhlin V. A new version of the fast multipole method for the laplace equation in three dimensions. Acta Numer 1997;6:229–69.

[16] Nishimura N, Yoshida K, Kobayashi S. A fast multipole boundary integral equation method for crack problems in 3D. Engng Anal Boundary Elem 1999;23:97–105.

[17] Peirce AP, Spottiswoode S, Napier JAL. The spectral boundary element method: a new window on boundary elements in rock mechanics. Int J Rock Mech Min Sci Abstr 1992;29:379–400.

[18] Love AEH. A treatise on the mathematical theory of elasticity. New York: Dover, 1944.

[19] Gray LJ, Martha Luiz F, Ingraffea AR. Hypersingular integrals in boundary element fracture analysis. Int J Numer Meth Engng 1990;29:1135–58.

[20] Lutz ED, Gray LJ. Exact evaluation of singular boundary integrals without CPV. Commun Numer Meth Engng 1993;9:909–15.

[21] Ioakimidis NI. A natural approach to the introduction of finite-part

integrals into crack problems of three-dimensional elasticity. Engng Fract Mech 1982;16:669–73.
[22] Ioakimidis NI. Exact expression for a two-dimensional finite part integral appearing during the numerical solution of crack problems in three-dimensional elasticity. Commun Appl Numer Meth 1985;1:183–9.
[23] Massimo Guiggiani. The evaluation of cauchy principal value integrals in the boundary element method — a review. Math Computer Model 1991;15:175–84.
[24] Tanaka M, Sladek V, Sladek J. Regularization techniques applied to boundary element methods. Appl Mech Rev 1994;47(10):457–99.
[25] Cruse TA, Richardson JD. Non-singular somigliana stress identities in elasticity. Int J Numer Meth Engng 1996;39:3273–304.
[26] Singular integrals in boundary element methods. In: Sladek V, Sladek J, editors. Advances in boundary elements, Computational Mechanics Publication, 1998.
[27] Richardson JD, Cruse TA. Weakly singular stress-BEM for 2D elastostatics. Int J Numer Meth Engng 1999;45(1):13–35.
[28] Saad Y, Shultz MH. GMRES: a generalized minimal residual algorithm for solving nonsymmetric linear systems. SIAM J Sci Statist Comput 1986;7:856–69.
[29] Barrett R, Berry M, Chan TF, Demmel J, Donato J, Dongarra J, Eijkhout V, Pozo R, Romine C, Van der Vorst H. Templates for the solution of linear systems: building blocks for iterative methods. 2nd ed. Philadelphia, PA: SIAM, 1994.
[30] Deb A, Banerjee PK. A comparison between isoparametric lagrangian elements in 2D BEM. Int J Numer Meth Engng 1989;28(7):1539–55.
[31] Richardson JD, Cruse TA, Huang Q. On the validity of conforming BEM algorithms for hypersingular boundary integral equations. Comput Mech 1997;20:213–20.
[32] Martin PA, Rizzo FJ, Cruse TA. Smoothness-relaxation strategies for singular and hypersingular integral equations. Int J Numer Meth Engng 1998;42:885–906.
[33] Brigham EO. The fast fourier transform and its applications. Englewood Cliffs, NJ, USA: Prentice Hall, 1988.
[34] Cooley JW, Tukey JW. An algorithm for the machine calculation of complex fourier series. Math Comput 1965;19:297–301.
[35] Zienkiewicz OC, Taylor RL. The finite element method. 4th ed. London: McGraw-Hill, 1994.
[36] Chien CC, Rajiyah H, Atluri SN. On the evaluation of hyper-singular integrals arising in the boundary element method for linear elasticity. Comput Mech 1991;8:57–70.
[37] Huang Q, Cruse TA. On the non-singular traction-BIE in elasticity. Int J Numer Meth Engng 1994;37:2041–72.
[38] Cruse TA, Suwito W. On the somigliana stress identity in elasticity. Comput Mech 1993;11:1–10.
[39] Timoshenko SP, Goodier JN. Theory of elasticity. 3rd ed. Mexico: McGraw-Hill, 1987.
[40] Higham NJ. Accuracy and stability of numerical algorithms. Philadelphia: SIAM, 1996.
[41] Lin YJ, Rudolphi TJ. New identities for fundamental solutions and their applications to non-singular boundary element formulations. Comput Mech 1999;24:286–92.